

# Experiments and Modeling of a Single Multicopter Rotor Response to Sinusoidal Vertical Gusts



A. D. Gardner\*  
Research Scientist



A. A. Kostek  
Research Scientist  
German Aerospace Center (DLR), Göttingen, Germany



F. Löble  
Research Scientist



J. N. Braukmann  
Research Scientist

This work is licensed under Creative Commons Attribution International License CC-BY

**Multicopters operate in environments subject to strongly gusting winds and need good aeromechanical models to improve the aircraft. A common, convenient, assumption is that the gusting inflow is quasi-static at each instant, but this assumption has never been tested. This paper shows that there is a solid physical basis for the simplified aerodynamic models of a single multicopter response to gusts. Experiments and computations show that using the static relationship between thrust or power and aerodynamic angle of attack for a single multicopter rotor (the quasi-static assumption) in sinusoidally pitching sideflow can be used to predict the thrust or power for unsteady variation of the angle of attack if the instantaneous flow angle of the freestream is known. Vertical (angle) gusts up to  $1885^\circ/\text{s}$  ( $k = 2.2$  based on the diameter) and with a wavelength longer than the rotor diameter were shown to be covered by this assumption.**

## Nomenclature

$c$	chord, m
$c_{75}$	chord at $r/R = 0.75$ (0.023 m)
$C_p$	power coefficient, $C_p = P/\rho\pi\Omega^3R^5$
$C_T$	thrust coefficient, $C_T = F/\rho\pi\Omega^2R^4$
$f$	frequency, Hz
$F$	thrust, N
$k$	reduced frequency, $k = \pi fL/v_\infty$
$L$	reference length for reduced frequency, m
$N_b$	number of blades, $N_b = 2$
$P$	mechanical power, W
$P_e$	electrical power, W
$Q$	torque, Nm
$r$	radial position, m
$R$	rotor radius, $R = 0.159$ m
$t$	time, s
$T$	gust period, s
$v_\infty$	freestream velocity, m/s
$\alpha$	angle of attack, $^\circ$
$\rho$	density, $= 0.129$ kg/m <sup>3</sup>
$\sigma$	rotor solidity, $\sigma = N_b c_{75}/\pi R$
$\Omega$	rotational frequency, $2\pi f$ , rad/s
CFD	computational fluid dynamics
DC	direct current
DLR	German Aerospace Center

LDA	laser doppler anemometry
RTG	rotor test facility Göttingen
UAV	unmanned aerial vehicle
UPM	unsteady panel method code of DLR

## Introduction

Multicopters of all sizes have recently been widely investigated for their potential in urban air mobility, transport, and inspection. Operating in an urban environment involves complex wind fields with transverse and longitudinal gusts around obstacles. Wind around buildings is commonly in the range of 5–10 m/s, with gusts up to 15 m/s (Ref. 1) and gust angles exceeding  $60^\circ$  angle of attack (Ref. 2). Strongly gusting flows have been shown to induce strong nonlinear unsteady effects on the aerodynamics of free-flying multicopters, probably due to flow separation, and it has been shown that nonlinear flight dynamics is necessary to accurately predict the gust response of an unmanned aerial vehicle (UAV) in this case (Ref. 3). This has been verified by a multicopter flying freely in flow generated using a series of large fans to produce repeatable wind gusts (Ref. 4). The effect of relatively mild gusts on multicopters is significant, with one study finding a 13% difference in power required compared with quiescent flow (Ref. 5). If a gust causes the rotor to have flow separation (Ref. 6), then the figure of merit will change significantly, as also seen in Ref. 7. It has been shown in a similar study to this one (Ref. 8) that longitudinal gusts (variation in velocity) have almost no effect on a rotor with KDE 12.5"  $\times$  4.3 blades in side flow, the same rotor as used in this study.

A convenient assumption is that the gusting inflow is equivalent to static flow at each instant and that the quasi-static flow over time is generated by chaining these static instants, but this assumption has never

Corresponding author; email: tony.gardner@dlr.de.

A version of this paper was presented at the Vertical Flight Society's 80th Annual Forum & Technology Display, Montréal, Québec, Canada, May 7–9, 2024. Manuscript received August 2024; accepted April 2025.

been tested. Despite this, most vehicle-level investigations into gust response of multicopters assume a quasi-static response in the rotor thrust (Refs. 9–12), meaning that the thrust changes in response to wind speed and direction, but follows the static polars and independently of gust frequency or ramping rate. The success of these latter approaches suggests that the aerodynamic thrust response of the rotors themselves is not dominated by unsteady aerodynamics, and this paper shows that there is a solid physical basis for the simplified quasi-static aerodynamic models of a single multicopter rotor response to gusts. This study only investigates the rotor operating in the linear region of fully attached flow.

Unsteady aerodynamics and even dynamic stall are common problems in the aerodynamics of vertical lift rotors (Refs. 13, 14), and additionally in flutter associated with aircraft wings (Ref. 15). In calculating the reduced frequency  $k = \pi f c / v_\infty$ , the value of  $v_\infty$  depends on the application. For fixed wings,  $v_\infty$  is the freestream speed. For rotary wings,  $v_\infty$  is the sum (or difference) of the freestream velocity and the blade rotational velocity. For helicopters, typically reduced frequencies based on the chord  $c$  and the  $1/\text{rev}$  cyclic pitching frequency  $f$  are below  $k = 0.2$ , whereas for aircraft wings in flutter, reduced frequencies can exceed  $k = 0.5$  (Ref. 16). Unsteady aerodynamics generally become important in the range  $k = 0.1$ – $0.3$ . There has been a large amount of literature investigating the unsteady response of a flying helicopter to various gust forms, for instance, flying in a ship's airwake (Refs. 17, 18), in the tip vortex of a preceding aircraft (Refs. 19, 20), or the wake of a wind turbine (Ref. 21). A helicopter has a flexible rotor system, and the scale of a helicopter rotor is large compared with the scale of the gusts in most of these studies. In contrast, a multicopter has stiff rotors in edgewise flow, is generally smaller than the oncoming gust wavelength, and the gust response appears from the literature to be primarily limited by the motor response to the step gust input (Ref. 22). It is not immediately clear whether the normalizing length for the reduced frequency is the rotor diameter (treating the rotor as a circular wing), or the rotor chord, which produces an order of magnitude difference in the computed reduced frequency.

The generation of transverse gusts is a common task in wind tunnel testing, which has not changed significantly in the last half century. A lifting body (airfoil or wing) is placed in the wind tunnel, and as the lift is varied the angle of the wake changes. The effect on the wake is described by Theodorsen's theory for unsteady aerodynamics and has been verified by many experiments (Ref. 23). The lift of the airfoil is varied by changing the angle of attack of the whole airfoil (Ref. 24) or of a flap (Ref. 25) or by combining pitching and plunging motion (Ref. 23). An array of vanes is often used to have a gust which is not contaminated by the vane boundary layer (Refs. 26, 27).

This paper uses a single multicopter rotor in vertical sinusoidal gusts, with a motor which accurately follows the prescribed rotation. This separated the aerodynamics from the dynamics of the motor control.

### Experimental Setup

The experiment used a two-bladed, fixed-pitch single multicopter rotor incorporating blades of type KDE 12.5"  $\times$  4.3 with 0.159 m radius and solidity 0.092 with edgewise flow into the rotor, with the same rotor unit setup as used in Refs. 7, 28, and 29. A new rotor head was designed, rather than the manufacturer's rotor head, so that the blade root was locked in position, eliminating vibrations caused by lead-lag movements. Physical constraints (Ref. 30) required the rotor to be mounted with the rotation axis horizontal, and a 180 W brushless DC motor with a rotation rate of 5400 RPM (90 Hz) was used for all test cases in this paper. The oncoming sinusoidal-type gust affects the angle of attack, with nose-up defined as positive, and nose-down as negative, with a mean flow velocity at the rotor position of 13.4 m/s. The tested conditions have a rotor advance ratio of 0.15 with a tip Mach number of 0.26 and Reynolds

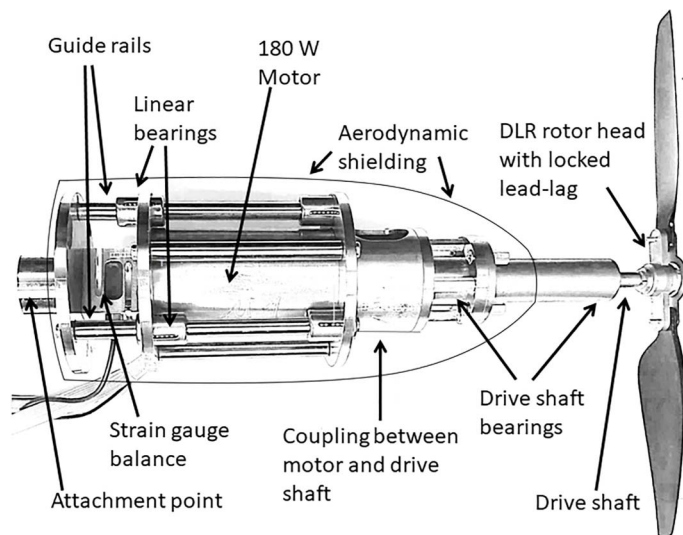


**Fig. 1. Single multicopter rotor, motor, and balance setup for the experiments.**

numbers of order 30,000 across the rotor disk. The experiments were conducted in the Rotor Test Facility Göttingen (RTG) of the German Aerospace Center (DLR). During the experiments, the rotor phase and rotation rate were monitored and were within  $1^\circ$  of the expected position of the rotor for a 90 Hz rotation rate at all times.

The setup is shown in Fig. 1, with the motor coupled to a drive shaft supported by separate bearings to decrease the blockage below the rotor. The axial force was measured using a single-axis strain gauge force link placed behind the motor, with the side forces and bending moments removed using a system of three rods on linear bearings. The force link was calibrated in situ and a worst-case accuracy of  $\pm 0.15$  N is expected. The electrical power ( $P_e$ ) of the rotor and control electronics is measured at the DC power supply, and then converted to mechanical power ( $P$ ) via a dynamometer calibration of the motor and controller for the power required for different torques at 90 Hz rotation frequency, resulting in

$$P = 0.93(P_e - 22.68) \quad (1)$$

which suggests a motor efficiency of 93% and control electronics using 22.68 W. This method has an expected stochastic error of  $\pm 1.5\%$ , and an additional systematic error due to the drive shaft bearings was not seen.

The motor and force sensor were covered by an aerodynamic fairing to minimize the aerodynamic interference. The rotor and drive unit were mounted on a rotatable platform, allowing adjustment of the angle of attack.  $0^\circ$  angle of attack was defined to be with the rotor edgewise to the mean inflow.

The gust generator was an array of four pitching airfoils (Ref. 31) mounted with the airfoil leading edge at the exit of a free-jet wind tunnel (see Fig. 2(a)). The nozzle was equipped with Seiferth wings at the nozzle outlet to suppress shear layer instability (Ref. 32). The carbon-fiber NACA0015 airfoils had a chord length of 0.25 m and a 1 mm trailing edge thickness. The airfoils were evenly spaced over the nozzle width of 1.200 m (separated by 0.300 m) and extended over the entire nozzle height of 1.600 m. The pitching motion was applied using a 90 Nm/3 kW Parker 190ST brushless torque motor and a feedback learning controller which matched the prescribed sinusoidal motion with an angular accuracy better than  $\pm 0.05^\circ$ . The motor and controller were previously used for a number of low-speed investigations into dynamic stalls on pitching airfoils and wings (Refs. 33, 34). The airfoils were actuated via a push rod at the lower end, and the motion was monitored at the lower and upper

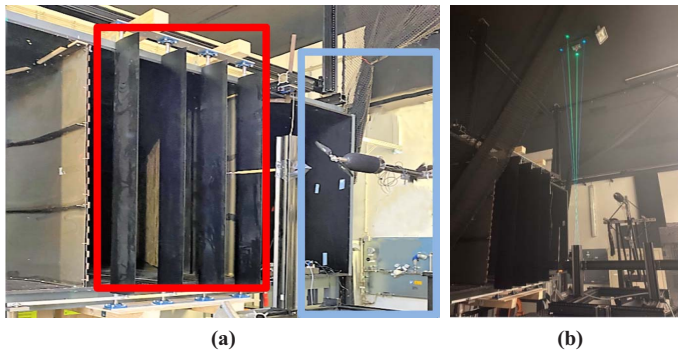


**Fig. 2. Test rig for sinusoidal vertical gusts: (a) pitching vanes (red box) and single multicopter rotor test rig (blue box) (Ref. 30) and (b) velocity measurement by LDA at the test position (Ref. 31).**

ends of the airfoils using laser distance measurement calibrated to the angle of attack with an accuracy of  $0.05^\circ$ . The lower end of the airfoil followed the prescribed motion precisely, and the maximum elastic twist of the airfoils at the opposite end to the drive was  $0.22^\circ$  at 5 Hz and  $\pm 10^\circ$  nominal angle of attack. At low frequencies, the entire free-jet of the wind tunnel is diverted with the gust generator, and at higher frequencies an oscillation is induced in the jet. The two sinusoidal vertical gusts used in this paper use an airfoil half-amplitude of  $10^\circ$ , with pitching frequencies of 1 and 5 Hz. The rotor rotation rate of 90 Hz means that at 5 Hz pitching frequency the rotor rotates 18 times for each input gust period.

Figure 2(b) shows the flow calibration using laser Doppler anemometry (LDA). For the experiments, the center of the rotor is 0.565 m behind the trailing edge of the airfoil, and vertically in the center of the 1.600 m wind tunnel height. The Dantec FiberFlow LDA probe was used in backscatter with a Dantec Dynamics BSA P80 burst spectrum analyzer. A 500 mm focal length lens and  $1 \mu\text{m}$  aerosolized di-ethyl-hexyl-sebacate droplets from a Laskin-nozzle seeding generator were used. The velocity in the flow direction was measured using the blue lasers and the crossflow using the green lasers. The LDA system only takes data when a valid point is detected; therefore, the two components take data independently at different nonequidistant rates. The settings included an offset in the acousto-optic modulator for the crossflow so that the positive and negative components were correctly measured. For all measured cases, a data validity of over 90% was achieved, and average data rates of around 800 Hz in the flow direction, and 250 Hz in the crossflow direction were measured. Data were taken for 1 min, and then the timescale was overlaid on a single period by using the modulus of the pitching period. The resulting data were smoothed using a top-hat 2moving average of  $1/250$  of the period time and then linearly interpolated onto a scale with 500 points per period. The two-dimensional (2D) LDA measurements (flow direction, cross-flow) were decomposed into flow angle, and flow velocity along the (varying) flow direction. The angular variation of the gust shapes in Fig. 3 is roughly sinusoidal and was fitted using a Fourier series of fifth order in sine and cosine (see Table 1). The pitching of the gust generators causes a  $2/\text{pitch}$  velocity fluctuation with respect to the mean of slightly over 2% (see Fig. 4); however, only the mean part of the flow velocity is treated in the following.

### Computations

The experiments were compared with computations using the unsteady free-wake panel method UPM with the setup used in Ref. 29 and validated against experiment, computational fluid dynamics (CFD), and a variety of midfidelity panel and lifting line codes. UPM, devel-

**Table 1. Vertical gust shapes (angle of attack in degrees) for UPM computations.**

Gust generator $k = 0.075$ (1 Hz)					
Function\Order	1	2	3	4	5
Sine	9.44	0.0032	-0.16	0.0087	-0.0021
Cosine	-0.18	0.026	0.048	0.12	0.024
Gust generator $k = 0.37$ (5 Hz)					
Function\Order	1	2	3	4	5
Sine	7.36	-0.16	-0.17	-0.072	-0.067
Cosine	0.20	0.085	-0.23	0.034	-0.021

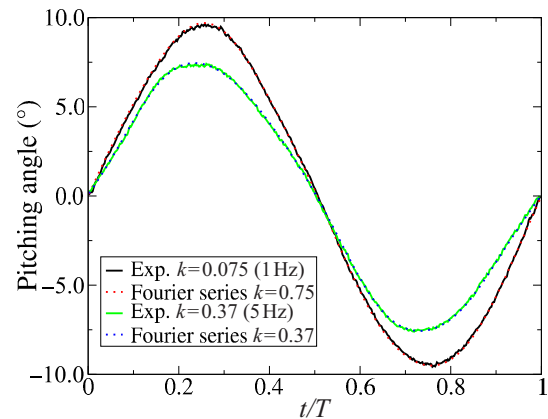


**Fig. 3. Gust angle at the measurement point (center of rotor position).**

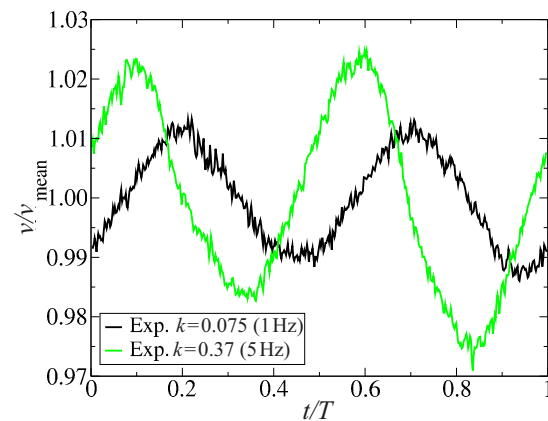


**Fig. 4. Gust velocity at the measurement point.**

oped at DLR, allows the simulation of flows with arbitrary body shapes (Refs. 35,36). Rigid body motion was used, and this is described in UPM via a series of stacked frames of reference so that the sinusoidal variation of the inflow was applied by adding an additional frame between the rotor translation through the air to produce forward flight and rotor head rotation frames.

The code solves potential flow, with a viscous correction applied to improve the estimation of torque values included in postprocessing (Ref. 37), changing the torque values reported but not the wake shape. The viscous correction uses a stripwise analysis of the rotor airfoil, computing 2D sections. The boundary layer method of Eppler (Ref. 38) is used with the  $e^n$  transition model of Arnal with  $n = 9$ . Lifting bodies in UPM are described explicitly as a set of airfoil contours spaced along the

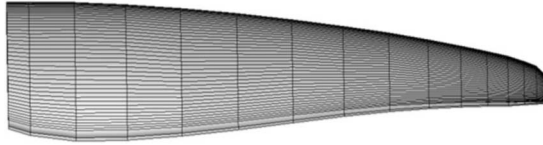


Fig. 5. UPM panel distribution on one of the two rotor blades (Ref. 29).

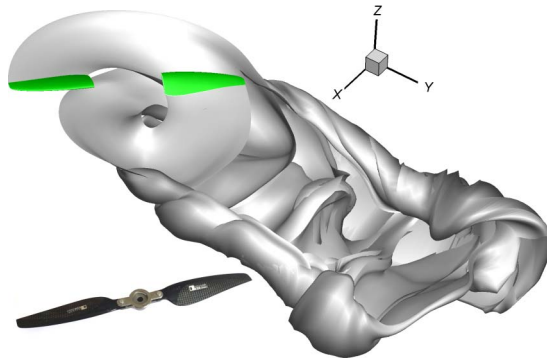


Fig. 6. UPM setup with wake from a pitching gust at  $k = 3.4$  (45 Hz) and real rotor including a hub in the insert bottom left.

length of a rotor blade or wing, in this case with 15 spanwise panels and 95 chordwise panels (see Fig. 5). The blade root is cut off, rather than being connected to the center, but this simplification was shown in the validation (Ref. 29) to produce acceptable results. The panel generation code PANGEN (a module of UPM) served in this study as a tool to prepare a computational model of a meshed blade with finite thickness and a sharp trailing edge. Sources and sinks of a priori unknown strengths are then distributed on the blade surface to enforce flow tangency to the surface at the control points. A doublet distribution along the chord simulates the lift distribution. The weighting function of doublet strength is prescribed and depends on the airfoil thickness. The flow field is assumed as subsonic and free of shocks with compressibility effects treated approximately using the Göthert rule (see Ref. 35).

An iterative scheme to ensure pressure equality at the trailing edge and satisfy the Kutta condition was applied in the calculations, by adding a short, zero-thickness panel at the airfoil trailing edge, along the bisector of the trailing edge. The orientation of the Kutta panel determines the direction of emission of a wake element at the time of its release from the blade trailing edge. After each computation step, a new free wake strip is created which is added to the previous wake. The singularity strengths evaluated for the Kutta panel determine the circulation of the vortices generated at each calculation step. The wake induction effect is included to satisfy the flow tangency condition for the next computation step. All the wake filaments are convected downstream after a computation step. The circulation of the wake row stays constant for the whole computation time; however, the vortices can freely deform according to the changes in the local velocity field. The full span free wake of the blades used a vortex lattice, which is truncated after three rotations.

UPM is computationally relatively efficient compared with CFD and has openMPI parallelization which can be used up to several hundred cores, which allows models with an increased number of wake and surface panels. For the computations in this paper, a constant timestep of  $2^\circ$  of azimuth was used for 170 rotor rotations. This used 12 h wall clock time on eight cores/eight threads of a desktop PC for each computation. The UPM setup is shown in Fig. 6, showing the hubless rotor modeled and the vortex lattice wake, compared to the real rotor in the bottom left.

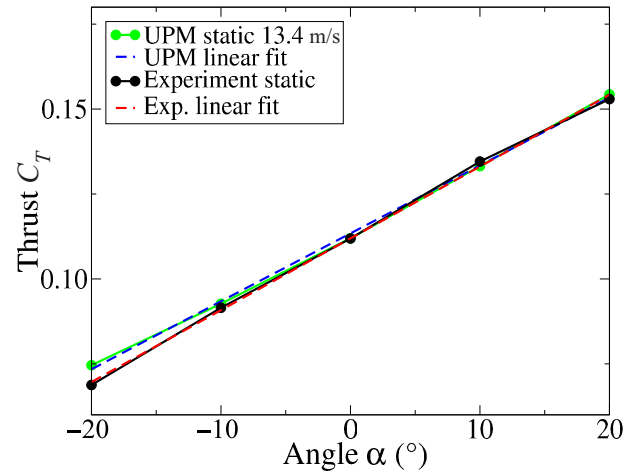


Fig. 7. Static polars for experiment and UPM with linear fits used for quasi-static thrust estimates at an inflow of 13.4 m/s.

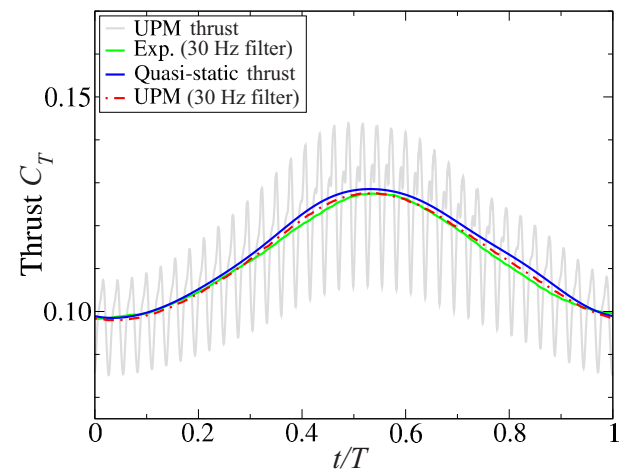


Fig. 8. Comparison of experiment with quasi-static prediction for gust frequency  $k = 0.37$  (5 Hz).

### Experimental Results

Figure 7 shows a static polar of rotor thrust. The experimental polar was produced by changing the rotor pitch angle while leaving the vanes of the gust generator at  $0^\circ$ . The experimental and numerical polars agree well with a difference in the range of 1–2%. They have different gradients; however, in the range of  $-10^\circ < \alpha < 10^\circ$ , the data were close enough that the fit from the numerical data was used for both:

$$C_T = 0.0020\alpha + 0.1134 \quad (2)$$

When using the function  $C_T = f(\alpha)$  to compute thrusts from a time sequence of angles of attack (in degrees) using the quasi-static assumption, Eq. (2) was used for the computations and experiment. The UPM computation was at 13.4 m/s, matched to the mean velocity of the gust flow experimental points.

Figure 8 shows a comparison between experimental and numerical results for the  $k = 0.37$  (5 Hz) gusts in Fig. 3, with the rotor fixed at  $0^\circ$ , and the gust generator moved at  $\pm 10^\circ$ . The experimental results were taken at a data rate of 10 kHz for 30 s, and phase-averaged with the gust frequency followed by a 30 Hz low-pass filter and is shown as the green line in Fig. 8. As the rotor rotates, the advancing blade sees a higher dynamic

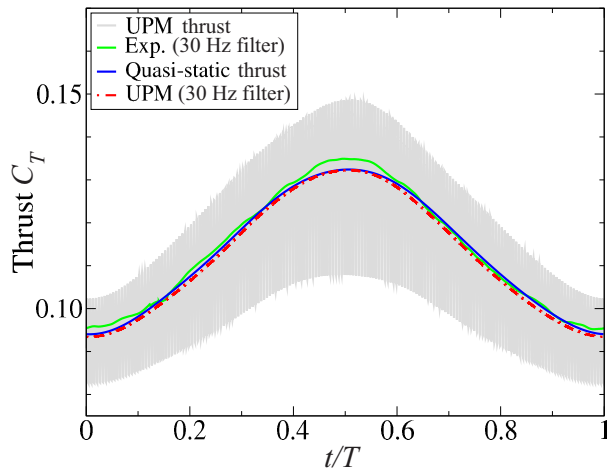


Fig. 9. Comparison of experiment with quasi-static prediction for gust frequency  $k = 0.075$  (1 Hz).

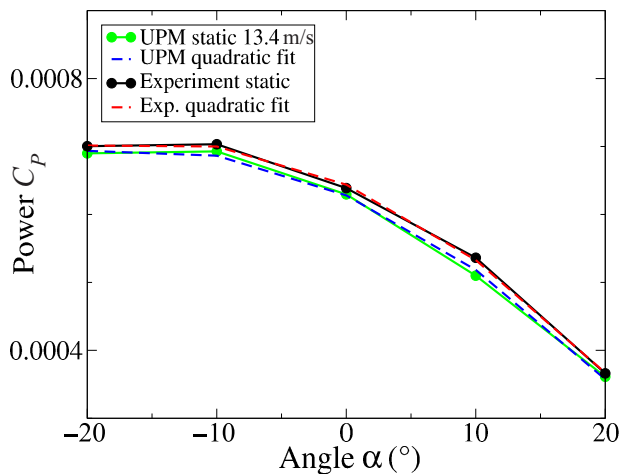


Fig. 10. Static polar calibration of the power curve for experiment and UPM.

pressure than the retreating blade, leading to a  $2/\text{rev}$  sinusoidal variation in axial force. The 30 Hz filter is used on the experimental data as the force balance in the experiment is mounted behind the motor (Fig. 1) and is not expected to resolve the force variation due to the blade passing. The combination of the motor mass and the balance stiffness causes vibration signals at the system eigenfrequencies in the range of 30–70 Hz, which do not reflect aerodynamic loads. These vibration signals are removed by low-pass filtering and do not offset the mean force measured. Also plotted in Fig. 8 (blue line) is the quasi-static prediction of thrust using the flow angle from the LDA calibration in Table 1 with the linear function from the static polar from Eq. (2). The phase of the quasi-static prediction is computed from the measured experimental instantaneous angle of the vanes, delayed by the distance between the quarter-chord position of the gust generator and the rotor center (0.752 m), divided by the mean flow velocity of 13.4 m/s. This was necessary because of a loss of synchronization between the LDA system and the vane angle-of-attack measurement during the calibration, meaning that only the shape and not the phase were measured during the calibration campaign. The agreement between the filtered experimental data and the quasi-static prediction of

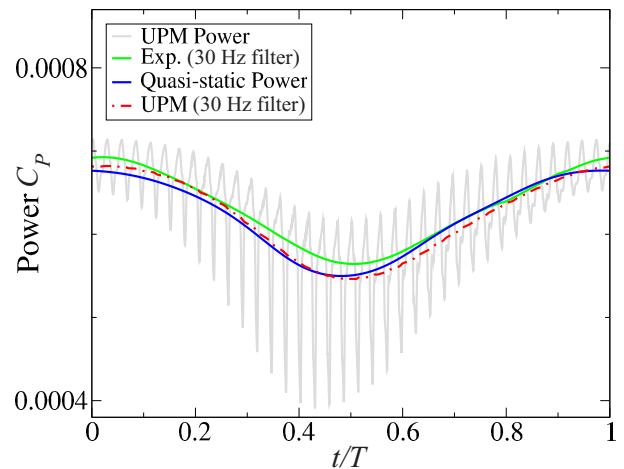


Fig. 11. Power for the test case at  $k = 0.37$  (5 Hz), experiment versus UPM.

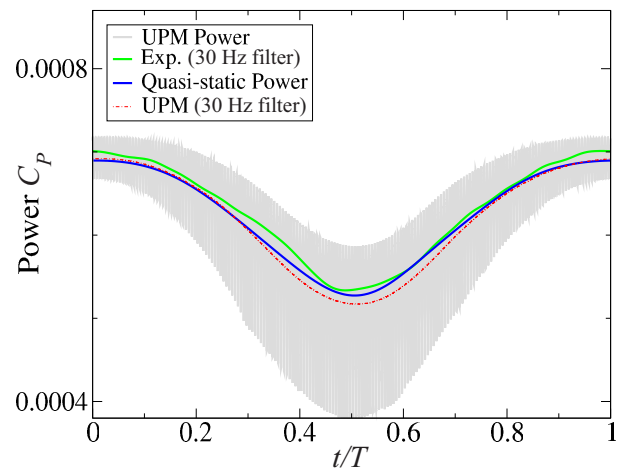


Fig. 12. Power for the test case at  $k = 0.075$  (1 Hz), experiment versus UPM.

thrust using the flow angle is good, indicating that no significant unsteady aerodynamics is present in this case.

Figure 8 also shows the instantaneous forces predicted by the UPM computations, with the gust shape of Table 1 as the gray line. The  $2/\text{rev}$  force variation caused by the two-bladed rotor is visible as a variation around the other lines. Also plotted in Fig. 8 are red-dotted UPM computations filtered by the same 30 Hz low-pass filter as used for the experiments. This agrees well with the 30 Hz low-pass filtered data from the experiment. Of these three groups of data (experiment, UPM, quasi-static), both the experiment and UPM potentially contain unsteady aerodynamic data, and the good agreement between these two datasets indicates that the experiment is well modeled by UPM. Additionally, the good agreement between these datasets and the quasi-static prediction indicates that no significant unsteady aerodynamic effects are present for this gust.

Equivalent data for a gust frequency of 1 Hz are shown in Fig. 9. The unfiltered numerical data are not well resolved in the image due to the relatively high frequency of the  $2/\text{rev}$  force peaks (180 Hz) compared with the gust frequency. However, the quasi-static prediction of thrust (blue line) matches the filtered UPM thrust data (red-dotted line) well. The conclusion from this comparison is also that no significant unsteady aerodynamic effects are present for this gust, as expected for a lower frequency

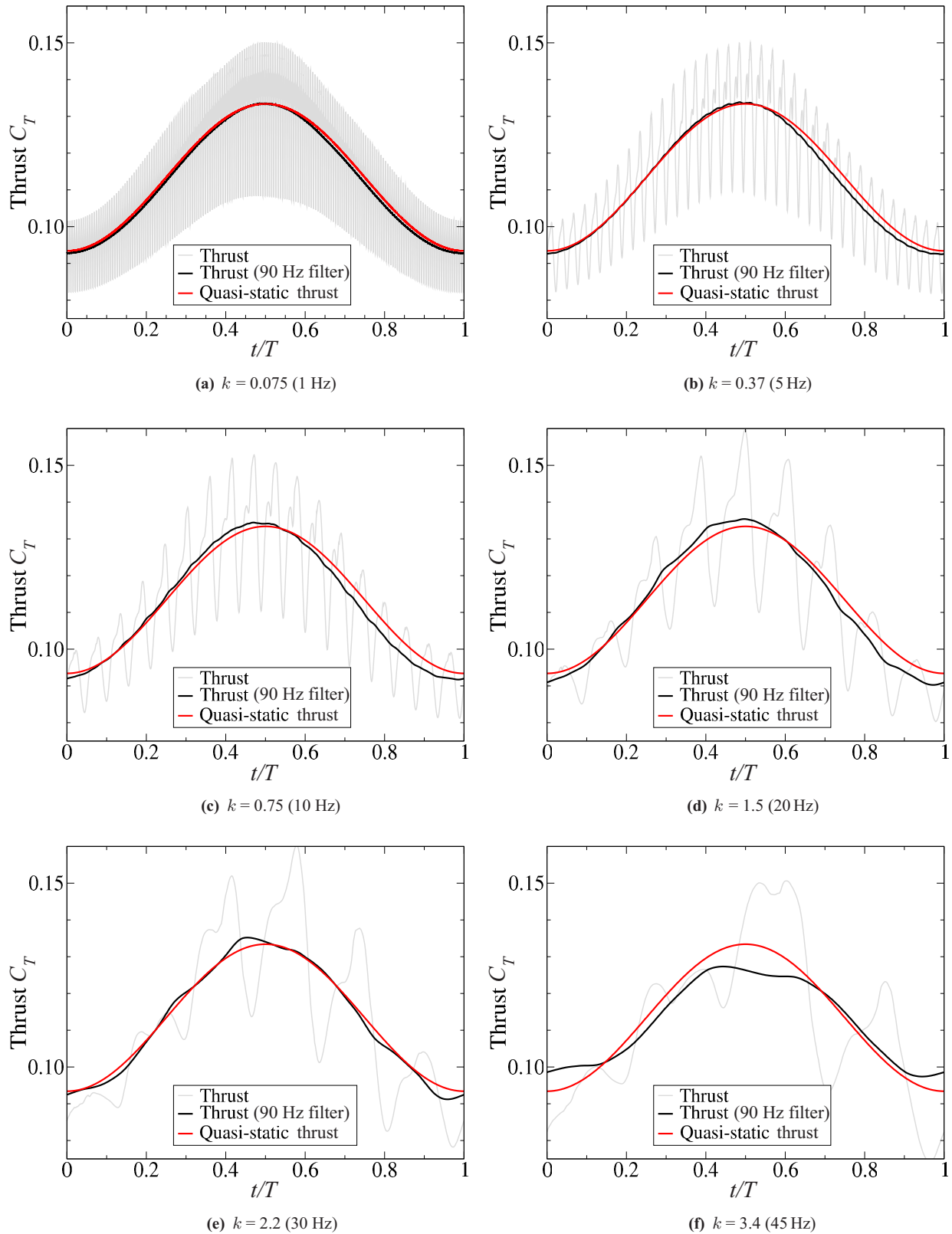


Fig. 13. UPM thrust versus quasi-static prediction of thrust with varying gust frequencies with a rotor at 5400 RPM (90 Hz).

than 5 Hz where this was already seen. The filtered experimental data also agree well with both the filtered UPM data and the quasi-static prediction. The reason for the excursion in the maximum thrust in the experimental data for  $k=0.075$  (1 Hz) is not clear, but this case is actually the experimentally more challenging of the two, due to the diversion of the entire wind-tunnel free-jet by the vanes, rather than the oscillation produced at  $k=0.37$  (5 Hz) where the jet does not have time to be diverted.

Figure 10 shows a static polar of the rotor power coefficient  $C_p$ . The experimental polar was produced by changing the rotor pitch angle while leaving the vanes of the gust generator at  $0^\circ$ . The measurement points are the same as in Fig. 7. The torque ( $Q$ ) is computed by UPM, adding the viscous correction in postprocessing to the torque computed by the potential solver, and is converted to mechanical power by  $P = Q\Omega$ . The electrical power is converted to mechanical power using Eq. (1) and filtered using a 30 Hz low-pass filter to be consistent with the treatment of thrust measurement. The polars in Fig. 10 show a good agreement between experimentally measured power and UPM prediction, with a difference in the range of 1–3%, resulting in the following quadratic fit from the numerical data (angle in degrees), analogue to the approach with the static thrust measurements:

$$C_p = -2.57 \times 10^{-7} \alpha^2 - 8.40 \times 10^{-6} \alpha + 6.44 \times 10^{-4} \quad (3)$$

In Fig. 11, the power is shown for the gust frequency of  $k=0.37$  (5 Hz). Analogue to the thrust, the instantaneous UPM power computation (gray line) shows a 2/rev variation in power. The UPM data filtered at 30 Hz (red dotted line) agree rather well with the quasi-static prediction of power from the flow angle (blue line) in Table 1 with the quadratic function from the static polar from Eq. (3). The agreement between experiment (green line) and quasi-static prediction is better during the downstroke (high angle produces high thrust using less power). This is not an increased amount of unsteady aerodynamics being present since the agreement between the quasi-static prediction and the UPM computation is good. The difference is actually due to increased experimental scatter in the measurement of power compared to the quasi-static prediction. This shows that the power can also be well predicted using the quasi-static assumption if the instantaneous flow angle of the freestream is known. Similarly, Fig. 12 shows a good agreement between the filtered experiment, filtered UPM power, and the quasi-static prediction of power from the flow angle.

### Extension to Higher Frequencies Using UPM

With the validation completed, UPM computations were used to extend the prediction to higher gust frequencies. For these computations, and for better generalizable results, a purely sinusoidal gust with a uniform gust amplitude of  $\pm 10^\circ$  was used rather than the fitted gusts used in the previous section. The sinusoidal gust is rather sharper at the peaks than the measured gust shape. Figure 13 compares thrusts computed using UPM with a quasi-static prediction. The quasi-static prediction used the rotor's instantaneous aerodynamic angle of attack (perfectly known in the UPM simulation) and the static calibration polar shown in the previous section. The instantaneous thrust is low-pass filtered at 90 Hz to remove the effects of rotor rotation. A higher filter frequency can be used here as the balance eigenfrequencies do not have to be avoided.

As expected for  $k=0.075$  (1 Hz) and  $k=0.37$  (5 Hz) (Figs. 13(a) and 13(b)), the rotor rotation rate is much faster than the gust frequency. The filtered UPM data (black line) compare well with the quasi-static prediction (red line). As the frequency increases to  $k=0.75$  (10 Hz) and  $k=1.5$  (20 Hz) (Figs. 13(c) and 13(d)), the rotation of the rotor starts to be of the same order as the gust frequency, and the filtering of the UPM data at

90 Hz no longer results in a smooth curve. Despite this, a good agreement between the filtered UPM data and the quasi-static prediction is seen on the upstroke, with a slightly worse agreement on the downstroke. There does not appear to be a phase offset which is increasing with increasing gust frequency, which is expected if an unsteady aerodynamic effect is present. Increasing the gust frequency further to  $k=2.2$  (30 Hz) and  $k=3.4$  (45 Hz) (Figs. 13(e) and 13(f)) shows relatively good agreement between the filtered UPM data at 30 Hz, but poorer agreement at 45 Hz, where the peaks of the thrust are cut off in the filtering. At this gust frequency, the filtering does not work well, since there are only two rotor rotations per gust. Additionally, the gust wavelength at 45 Hz is 0.30 m, in the same order as the rotor diameter. In summary, the quasi-static assumption gives a good approximation of the filtered thrust up to a gust frequency of  $k=2.2$  (30 Hz). At 30 Hz and amplitude  $10^\circ$ , the maximum pitching rate is  $1885^\circ/\text{s}$ .

In this paper, the rotor diameter is used as a normalizing length for the reduced frequency. Both the maximum  $k=0.37$  computed for the experiments and the maximum  $k=2.2$  for the computations should be expected to show significant unsteady aerodynamics. This would indicate that calculating reduced frequency based on the circular wing assumption does not produce  $k$ -values, which well predict unsteady effects. This means that the normalizing length for predicting unsteady effects from reduced frequency is shorter than the rotor diameter. For the case of  $k=2.2$  based on the gust frequency and the diameter of the rotor for a gust at 30 Hz, if we instead use the rotor chord as a normalizing length, much lower reduced frequencies are calculated. The reduced frequency  $k = \pi fc/v_\infty$  of the rotor blade sections due to the rotation is  $k=0.04$  at  $r/R=0.5$  ( $c=0.032$  m) or  $k=0.2$  at  $r/R=1$  ( $c=0.012$  m), based on the rotation rate and local blade chord (see Ref. 29 for geometry).

### Conclusion

Experiments and computations with a free-wake panel code were performed for a stiff single multicopter rotor subjected to a sinusoidal pitching gust. The agreement between the experiment and panel computation was good, both for thrust and for power. Both power and thrust were well predicted by a static polar calibration of the rotor and computing the thrust/power from a known instantaneous flow angle of the freestream for gust cases. This indicates that unsteady aerodynamics do not play a significant role in the rotor aerodynamics at these pitching rates and that the normalizing length for predicting unsteady effects from reduced frequency is shorter than the rotor diameter. Sinusoidal vertical gusts up to  $1885^\circ/\text{s}$  ( $k=2.2$  based on the diameter) were shown to be covered by this assumption. This shows that there is a solid physical basis for the simplified aerodynamic models used by many authors for the prediction of a single multicopter rotor response to gusts with a wavelength longer than the rotor diameter.

### Acknowledgments

This research was funded by the DLR Project URBAN-Rescue, with funding from the German Federal Ministry for Economic Affairs and Climate Action (BMWK). A. Kostek was funded by a DLR-DAAD Scholarship.

### References

- <sup>1</sup>Gross, G., "On the Estimation of Wind Comfort in a Building Environment by Microscale Simulation," *Meteorologische Zeitschrift*, Vol. 23, (1), pp. 51–62, 2014, DOI: 10.1127/0941-2948/2014/0577.
- <sup>2</sup>Ahmad, N., Inagaki, A., Kanda, M., Onodera, N., and Aoki, T., "Large-Eddy Simulation of the Gust Index in an Urban Area Using

the Lattice Boltzmann Method,” *Boundary-Layer Meteorology*, **163**, 447–467 (2017), DOI: 10.1007/s10546-017-0233-6.

<sup>3</sup>Park, S. H., Lee, S., Im, B., Lee, D., and Shin, S. J., “Improvement of a Multi-Rotor UAV Flight Response Simulation Influenced by Gust,” *Aerospace Science and Technology*, **134**, 108156 (2023), DOI: 10.1016/j.ast.2023.108156.

<sup>4</sup>McCrink, M., Seth, D., and Herz, S., “Quadrotor Performance Measurement During Wake and Gust Encounters,” Proceedings of the AIAA AVIATION 2022 Forum, June 27–July 1, 2022, DOI: 10.2514/6.2022-4064.

<sup>5</sup>Kim, H., Lim, D., and Yee, K., “Flight Control Simulation and Battery Performance Analysis of a Quadrotor under Wind Gust,” Proceedings of the 2020 International Conference on Unmanned Aircraft Systems (ICUAS), Athens, Greece, September 1–4, 2020.

<sup>6</sup>Murakami, M., Abe, H., Aono, H., and Ishikawa H., “Effects of Gust Flow on Aerodynamic Performance of Multirotor Drone Propellers in Hovering Flight,” *Journal of Fluid Science and Technology*, **17**, JFST0013 (2022), DOI: 10.1299/jfst.2022jfst0013.

<sup>7</sup>Löbke, F., Kostek, A. A., Schwarz, C., Schmid, R., Gardner, A. D., and Raffel, M., “Aerodynamics of Small Rotors in Hover and Forward Flight,” Proceedings of the 48th European Rotorcraft Forum, Winterthur, Switzerland, September 5–9, 2022.

<sup>8</sup>Cai, J., and Gunasekaran, S., “Sinusoidal Gust Response of RC Propellers Tandem Configuration,” Proceedings of the 79th Annual Forum of the Vertical Flight Society, West Palm Beach, FL, May 16–18, 2023, DOI: 10.4050/F-0079-2023-17981.

<sup>9</sup>Suárez Fernández, R. A., Dominguez, S., and Campoy, P., “L1 Adaptive Control for Wind Gust Rejection in Quad-Rotor UAV Wind Turbine Inspection,” Proceedings of the 2017 International Conference on Unmanned Aircraft Systems (ICUAS), Miami, FL, 2017, pp. 1840–1849, DOI: 10.1109/ICUAS.2017.7991485.

<sup>10</sup>Yeo, D., Hrishikeshavan, V., and Chopra, I., “Gust Detection and Mitigation on a Quad Rotor Biplane,” Proceedings of the AIAA Atmospheric Flight Mechanics Conference, San Diego, CA, January 4–8, 2016, DOI: 10.2514/6.2016-1531.

<sup>11</sup>Whidborne, J. F., and Cooke, A. K., “Gust Rejection Properties of VTOL Multirotor Aircraft,” *IFAC-PapersOnLine*, Vol. 50, (2), 2017, pp. 175–180, DOI: 10.1016/j.ifacol.2017.12.032.

<sup>12</sup>Wang, B., Ali, Z. A., and Wang, D., “Controller for UAV to Oppose Different Kinds of Wind in the Environment,” *Journal of Control Science and Engineering*, **2020**, 5708970 (2020), DOI: 10.1155/2020/5708970.

<sup>13</sup>Leishman, J. G., *Principles of Helicopter Aerodynamics*, Cambridge University Press, New York, NY, 2006.

<sup>14</sup>Gardner, A. D., Jones, A. R., Mulleners, K., Naughton, J. W., and Smith, M. J., “Review of Rotating Wing Dynamic Stall: Experiments and Flow Control,” *Progress in Aerospace Sciences*, **137**, 100887 (2023), DOI: 10.1016/j.paerosci.2023.100887.

<sup>15</sup>Chai, Y., Gao, W., Ankay, B., Li, F., and Zhang, Ch., “Aeroelastic Analysis and Flutter Control of Wings and Panels: A Review,” *International Journal of Mechanical System Dynamics*, Vol. 1, (10), 2021, pp. 5–34, DOI: 1002/msd.12015.

<sup>16</sup>Dietz, G., Schewe, G., and Mai, H., “Experiments on Heave/Pitch Limit-Cycle Oscillations of a Supercritical Airfoil Close to the Transonic Dip,” *Journal of Fluids and Structures*, Vol. 19, (1), 2004, pp. 1–16, DOI: 10.1016/j.jfluidstructs.2003.07.019.

<sup>17</sup>Štrbac, A., Maibach, M.-J., Greiwe, D., Kalra, A., and Gardner, A. D., “Evaluation of Pilot Assistance Systems for Helicopter Ship Deck Landing,” Proceedings of the 78th Annual Forum of the Vertical Flight Society, Fort Worth, TX, May 10–12, 2022, DOI:10.4050/F-0078-2022-17545.

<sup>18</sup>Scott, P., White, M. D., and Owen, I., “The Effect of Ship Size on Airwake Aerodynamics and Maritime Helicopter Operations,” Proceedings of the 41st European Rotorcraft Forum, Munich, Germany, September 1–4, 2015.

<sup>19</sup>van der Wall, B. G., and van der Wall, L. B., “Analytic Solution of In-Plane Vortex-Rotor Interactions with Arbitrary Orientation and Its Impact on Rotor Trim,” *CEAS Aeronautical Journal*, Vol. 12, (3), pp. 519–534, 2021, DOI: 10.1007/s13272-021-00506-w.

<sup>20</sup>Whitehouse, G. R., and Brown, R. E., “Modelling a Helicopter Rotor’s Response to Wake Encounters,” *The Aeronautical Journal*, Vol. 108, (1079), pp. 15–26, 2004, DOI: 10.1017/S000192400004954.

<sup>21</sup>van der Wall, and Berend, G., “Potential Hazards of Wind Turbine Wake Vortices for Ultra-Light Sports Rotorcraft,” in *New Results in Numerical and Experimental Fluid Mechanics XII*, edited by A., Dillmann, G. Heller, E. Krämer, C. Wagner, C. Tropea, and S. Jakirlić. Notes on Numerical Fluid Mechanics and Multidisciplinary Design, Vol 142. Springer, Cham, Switzerland, pp. 830–840, 2019, DOI: 10.1007/978-3-030-25253-3\_78.

<sup>22</sup>Bahr, M., McKay, M., Niemiec, R., and Gandhi, F., “Handling Qualities of Fixed-Pitch, Variable-Speed Multicopters for Urban Air Mobility,” *The Aeronautical Journal*, Vol. 126, pp. 952–972, 2022, DOI:10.1017/aer.2021.114.

<sup>23</sup>Wei, N. J., Kissing, J., and Tropea, C., “Generation of Periodic Gusts with a Pitching and Plunging Airfoil,” *Experiments in Fluids*, **60**, 166 (2019), DOI: 10.1007/s00348-019-2815-1.

<sup>24</sup>Wade, W. F., “Experimental Generation and Investigation of a Sinusoidally Varying Gust,” Master Thesis, University of Michigan, 1958, <http://hdl.handle.net/10945/26534>.

<sup>25</sup>Umbarger, R. M., “Wind Tunnel Gust Simulation,” Master Thesis, Princeton University, 1970, <http://hdl.handle.net/10945/15219>.

<sup>26</sup>French, A., Friess, W., Goupee, A., and Berube, K., “Design, Construction and Evaluation of an Oscillating Vane Gust Generator for Atmospheric Flow Simulation,” *Wind*, Vol. 1, (1), pp 63–76, 2021. DOI: 10.3390/wind1010004.

<sup>27</sup>Saddington, A., Finnis, M., and Knowles, K., “The Characterisation of a Gust Generator for Aerodynamic Testing,” *Proceedings of the Institution of Mechanical Engineers, Part G: Journal of Aerospace Engineering*, Vol. 229, (7), pp. 1214–1225, 2015, DOI:10.1177/0954410014548237.

<sup>28</sup>Kostek, A. A., Braukmann, J. N., Löbke, F., Miesner, S., Visingardi, A., Boisard, R., Riziotis, V., Kßler, M., and Gardner, A. D., “Experimental and Computational Investigation of Aerodynamic Interactions in Quadrotor Configurations,” *Journal of the American Helicopter Society*, **69**, 022009 (2024), DOI: 10.4050/JAHS.69.022009.

<sup>29</sup>Kostek, A. A., Löbke, F., Wickersheim, R., Keßler, M., Boisard, R., Reboul, G., Visingardi, A., Barbarino, M., and Gardner, A. D., “Experimental Investigation of UAV Rotor Aeroacoustics and Aerodynamics with Computational Cross-Validation,” *CEAS Aeronautical Journal*, Vol. 15, pp. 643–658, 2023, DOI: 10.1007/s13272-023-00680-z.

<sup>30</sup>Bayer, J., “Untersuchung eines neuen Böen-Generators für den RTG-Windkanal,” [Investigation of a New Gust Generator for the RTG Wind Tunnel]. Master Thesis, TU Braunschweig, 2022.

<sup>31</sup>Gardner, A. D., “Commissioning Report for the RTG Gust Generator,” DLR Internal Report, DLR-IB-AS-GO-2022-165, 2022.

<sup>32</sup>Seiferth, R., “Vorausberechnung und Beseitigung der Schwingungen von Freistrah-Windkanälen,” *Monographien über Fortschritte der deutschen Luftfahrtforschung seit 1939*, Aerodynamische Versuchsanstalt Göttingen, 1946.

<sup>33</sup>Gardner, A. D., Merz, C. B., and Wolf, C. C., “Effect of Sweep on a Pitching Finite Wing,” *Journal of the American Helicopter Society*, **64**, 032007 (2019), DOI: 10.4050/JAHS.64.032007.

<sup>34</sup>Gardner, A. D., Wolf, C.C., and Raffel, M., “A New Method of Dynamic and Static Stall Detection Using Infrared Thermography,” *Experiments in Fluids*, **57**, 149 (2016), DOI: 10.1007/s00348-016-2235-4.

<sup>35</sup>Ahmed, S. R., and Vidjaja, V. T., “Unsteady Panel Method Calculation of Pressure Distribution on BO105 Model Rotor Blades,” *Journal of the American Helicopter Society*, Vol. 43, (1), pp. 47–56, 1998, DOI: 10.4050/JAHS.43.47.

<sup>36</sup>Yin, J., and Ahmed, S. R., “Helicopter Main-Rotor/Tail-Rotor Interaction,” *Journal of the American Helicopter Society*, Vol. 45, (4), pp. 293–302, 2000, DOI: 10.4050/JAHS.45.293.

<sup>37</sup>Johnson W., *Helicopter Theory*, Dover Publications, Inc., New York, 1980.

<sup>38</sup>Kunze, P., “Approximate Boundary Layer Methods for a 3D Panel Code for Helicopter Simulations,” Proceedings of the 19th ONERA-DLR Aerospace Symposium, Meudon, France, June 3–5, 2019.